METALLURGY

Multicomponent intermetallic nanoparticles and superb mechanical behaviors of complex alloys

T. Yang[1,2], Y. L. Zhao[2], Y. Tong[2], Z. B. Jiao[3], J. Wei[2], J. X. Cai[4], X. D. Han[4], D. Chen[2], A. Hu[2], J. J. Kai[2], K. Lu[5], Y. Liu[6], C. T. Liu[1,2]*

Alloy design based on single–principal-element systems has approached its limit for performance enhancements. A substantial increase in strength up to gigapascal levels typically causes the premature failure of materials with reduced ductility. Here, we report a strategy to break this trade-off by controllably introducing high-density ductile multicomponent intermetallic nanoparticles (MCINPs) in complex alloy systems. Distinct from the intermetallic-induced embrittlement under conventional wisdom, such MCINP-strengthened alloys exhibit superior strengths of 1.5 gigapascals and ductility as high as 50% in tension at ambient temperature. The plastic instability, a major concern for high-strength materials, can be completely eliminated by generating a distinctive multistage work-hardening behavior, resulting from pronounced dislocation activities and deformation-induced microbands. This MCINP strategy offers a paradigm to develop next-generation materials for structural applications.

High-performance materials with gigapascal strengths and large ductility are highly desirable for enhancing engineering reliability and energy efficiency, as well as reducing CO_2 emissions for material production. However, developing advanced materials with a substantial improvement of both strength and ductility is highly challenging because of strength and ductility's mutually exclusive relationship (1). Single-phase alloys usually display a good ductility but relatively low strengths. The introduction of nanotwins and transformation-induced martensites has shown their capability of giving a combined increase of strength (2, 3). However, the yield strength obtained from these approaches remains limited, which is generally insufficient for structural applications. Second-phase intermetallic compounds (IMCs) provide an efficient approach for enhancing alloy strengths (4, 5); however, most IMCs with atomically or-

dered structures are intrinsically brittle. The gain of gigapascal strengths by introducing high-density IMCs invariably leads to a reduced resistance to fracture. The highly reactive elements, such as Al in the Ni_3Al intermetallic phase, will also increase the susceptibility of these intermetallics to moisture-induced environmental embrittlement and further lower their tensile ductility (6, 7). Moreover, the microstructural heterogeneity of IMCs tends to introduce a localized stress-strain concentration and trigger microcracks under loading (8). Consequently, the early onset of plastic instability leads to a catastrophic failure of these materials.

Conventional alloy design based on single–principal-element alloy systems cannot break through this thorny dilemma, because of the limited abilities for further optimizing alloy chemistries and microstructures. Recently proposed metallurgical design in multi–principal-element alloy systems offers a promising pathway to alleviate these concerns (2, 9–12). Nevertheless, the results obtained so far have been disappointing at ambient temperatures, at which high-strength

[1]Department of Material Science and Engineering, College of Science and Engineering, City University of Hong Kong, Hong Kong, China. [2]Center for Advanced Structural Materials/Department of Mechanical Engineering, College of Science and Engineering, City University of Hong Kong, Hong Kong, China. [3]Department of Mechanical Engineering, Hong Kong Polytechnic University, Hong Kong, China. [4]Institute of Microstructure and Properties of Advanced Materials, Beijing University of Technology, Beijing 100124, China. [5]Shenyang National Laboratory for Materials Science, Institute of Metal Research, Chinese Academy of Sciences, Shenyang 110016, China. [6]The State Key Laboratory of Powder Metallurgy, Central South University, Changsha 410083, Hunan, China.
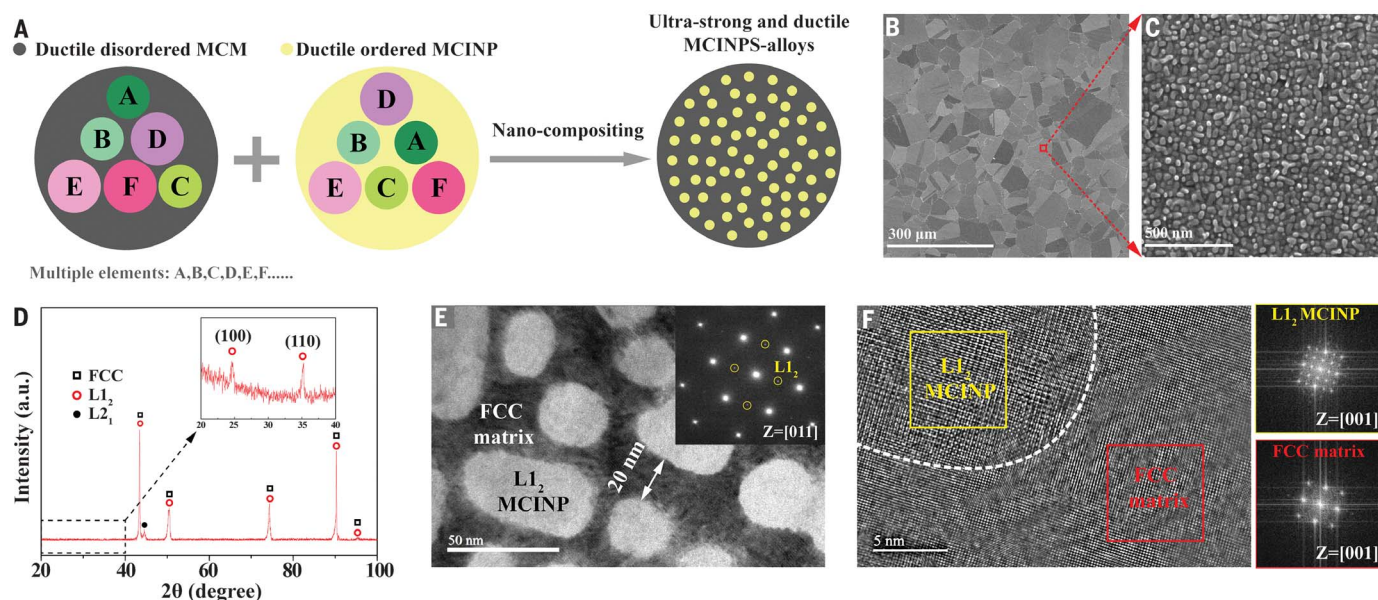*Corresponding author. Email: chainliu@cityu.edu.hk

Fig. 1. Conceptual design and microstructural characterizations of the MCINPS alloys. (**A**) Schematic of the design concept of the MCINPS alloys. MCM, multicomponent matrix. (**B**) Scanning electron microscopy (SEM) image of the Al7Ti7 alloy exhibiting the typical equiaxed grain structures. (**C**) SEM image of the Al7Ti7 alloy revealing the uniform distribution of high-density $L1_2$ MCINP within the grain interior. (**D**) XRD patterns showing the phase compositions of the Al7Ti7 alloy. a.u., arbitrary units. (**E**) TEM image of the Al7Ti7 alloy showing the nanostructured morphology. The inset shows the corresponding SAED pattern. (**F**) Representative high-resolution TEM image confirming the interfacial coherency.
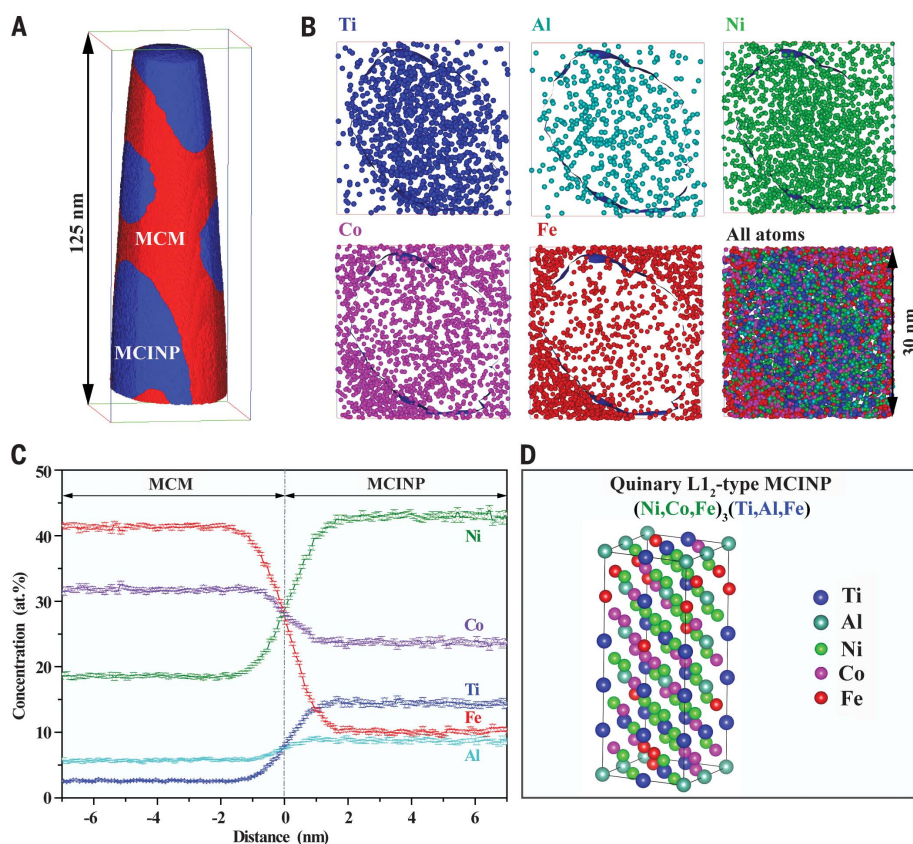
Fig. 2. Spatial morphology and multi-component nature of the MCINPs.
(**A**) 3D reconstruction map of an APT needle tip confirming the nanocomposited microstructure of the Al7Ti7 alloy. (**B**) High-resolution atom maps showing the atomistic distribution within the L1$_2$ MCINP of the Al7Ti7 alloy. (**C**) Proximity histogram across the matrix and nanoparticles revealing the multicomponent nature of the MCINPs of the Al7Ti7 alloy. (**D**) Ordering crystallographic structure and site occupancy of the L1$_2$ MCINP by density functional theory (DFT) calculations of the Al7Ti7 alloy.

ductility enhancement has not been realized yet. A typical example is the IMC hardening in face-centered cubic (fcc) high-entropy alloys (HEAs), in which the fcc-HEA matrix with a high work-hardening capability can suppress crack propagation and promote a retention of ductility only to a limited extent (*13–15*). Thus, when the yield strength of these alloys reaches up to 1 GPa, their tensile elongation is reduced substantially, far below what can be achieved in the freestanding fcc-type HEAs (*14*).

In this study, we developed an innovative design strategy to eliminate ductility loss in gigapascal-strength alloys. Our design concept aims to controllably create the ductile multi-component intermetallic nanoparticles (MCINPs) for coherent strengthening in the fcc-type HEA systems (Fig. 1A), in which we achieved in situ ductilization with a nanoscale precipitation of MCINPs by controlling the order-disorder phase transformation and elemental partition. Such conceptual design enables us not only to fully exert the strengthening effect of intermetallic nanoparticles but also to maintain a high work-hardening rate and plastic deformation stability. As a result, our MCINP-strengthening (MCINPS) alloys have achieved an exceptional strength-ductility combination without encountering the common problems of early local necking and limited uniform ductility.

We designed a series of MCINPS alloys, but, because of the page limitation, we only focus on two model alloys, (FeCoNi)$_{86}$-Al$_7$Ti$_7$ (Al7Ti7) and (FeCoNi)$_{86}$-Al$_8$Ti$_6$ (Al8Ti6), to illustrate the proof of concept based on systematic thermodynamic calculations (fig. S1 and table S1). By highly alloying with Ti and Al additions, we successfully introduced high-density L1$_2$ intermetallic nanoparticles in the FeCoNi-base alloy systems. In this approach, we selected the FeCoNi for the matrix to achieve a large "FCC+L1$_2$" dual-phase region for a dense precipitation. The partial partitioning of Fe and Co atoms into the L1$_2$ phase (table S1) helped to improve the intrinsic ductility of the L1$_2$ intermetallic phase (*6, 7*). Also, we reduced the propensity for environmental embrittlement (*6, 7*) of the alloys by adding Ti to reduce the Al content in the L1$_2$ intermetallic phase (*16*). These bulk nanocomposited MCINPS alloys were prepared by arc melting and followed by thermomechanical treatments. The typical polycrystalline structures we identified were composed of uniform equiaxed grains (about 40~50 μm) (Fig. 1B). Within the grain interior, the near-spherical MCINPs (about 30~50 nm) were uniformly distributed in the matrix with a high volume fraction up to 50 to 55% (Fig. 1C). We characterized the fcc-L1$_2$ dual-phase nanostructures, as shown in Fig. 1D, with x-ray diffraction (XRD). We detected only a very small amount (~0.3%) of submicrometer L2$_1$-phase precipitates at grain boundaries (fig. S2). We conducted electron backscattered diffraction (EBSD), which indicated a homogeneous and fully recrystallized microstructure

with a random distribution of various oriented grains in both Al7Ti7 and Al8Ti6 alloys (figs. S3 to S5). We found that the MCINPs were perfectly coherent with the matrix from transmission electron microscopy (TEM), selected-area electron diffraction (SAED), high-resolution TEM, and fast Fourier transformation (Fig. 1E). We determined a small lattice mismatch of the MCINP-matrix interface of ~0.21% for the Al7Ti7 alloy and ~0.16% for Al8Ti6 (fig. S6), dependent on the alloy composition. The small values of the lattice mismatch effectively enhance the nanoscale stabilization of the MCINPs without any heterogeneous coarsening (*8, 17, 18*).

We observed typical microstructural features (Fig. 2A) with a clear elemental partition between the matrix and MCINPs (Fig. 2, B and C, and table S2). The Ti and Al atoms occupied the B site of the L1$_2$ phases with a close-packed A$_3$B-type crystal structure. The Ni atoms occupied the A site (*18, 19*), whereas the Fe and Co atoms could occupy both sites, depending on the chemical composition (*6, 20*). It is possible that 2 atomic % (at %) of Fe or Co atoms can enter the B sublattice, as the sum of Ti and Al atoms is only ~23 instead of 25 at % (Fig. 2C and table S2). We performed first-principles calculations in 80-atom supercells (35 Ni, 7 Al, 11 Ti, 19 Co, and 8 Fe atoms) on the basis of the atom probe tomography (APT) compositional analysis. We constructed two L1$_2$-ordered models based on the (Ni$_{35}$Co$_{17}$Fe$_8$)(Al$_7$Ti$_{11}$Co$_2$) composition with
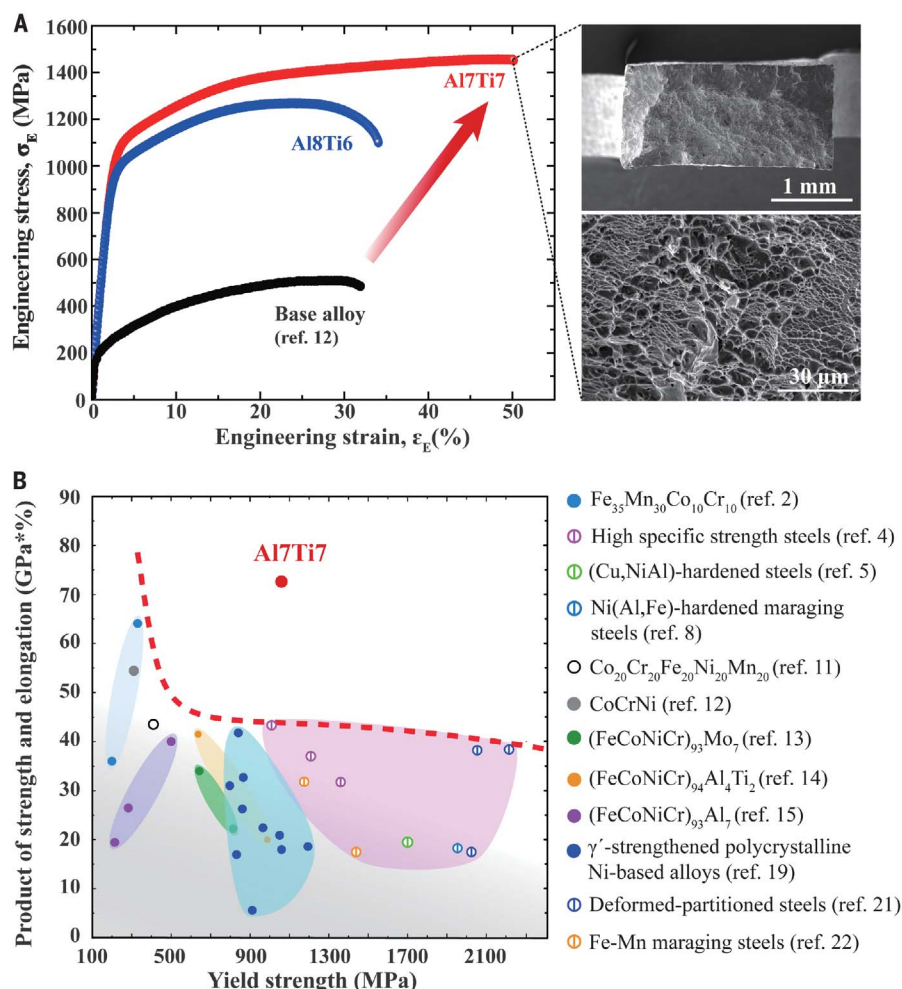
Fig. 3. Exceptional strength-ductility combination achieved in the MCINPS alloys at ambient temperature. (**A**) Engineering stress-strain curves of the MCINPS alloys compared with the FeCoNi base alloy (*12*), showing a significant increase of strength without ductility reduction. The Al7Ti7 alloy exhibits ductile dimpled structures without macroscopic necking. (**B**) Yield strength versus the product of strength and ductility of the MCINPS alloys compared with those of other high-performing materials (*2, 4, 5, 8, 11, 13, 14, 19, 21, 22*).

2 at % Co occupying the B sublattice and the $(Ni_{35}Co_{19}Fe_6)(Al_7Ti_{11}Fe_2)$ composition with 2 at % of Fe occupying the B sublattice. The model with Fe in the B site had a lower formation energy of -0.025 eV atom^{-1}, supporting that Fe occupies on the B sublattice (fig. S7). Thus, we identified the L1$_2$-type MCINPs as the quinary $(Ni_{43.3}Co_{23.7}Fe_8)_3(Ti_{14.4}Al_{8.6}Fe_2)$ phase (Fig. 2D), which had a major impact on the mechanical response of the present alloys.

Furthermore, we measured the engineering stress-strain curves of our MCINPS alloys at ambient temperature (Fig. 3A and table S3). The main concern regarding the traditional alloy design with a high density of IMCs is severe embrittlement. Our MCINPS alloys had a tensile yield strength (σ_Y) as high as 1 GPa and an ultimate tensile strength (σ_{UTS}) of ~1.5 GPa while having a ductility of up to ~50% as the tensile elongation. The local necking in the Al7Ti7 alloy was suppressed, and the strength was five times higher than that of the single-phase FeCoNi-based alloy

(*12*) (Fig. 3A). The Al7Ti7 alloy still showed a superb work-hardening ability ($\sigma_{UTS} - \sigma_Y = 440$ MPa, $\sigma_Y/\sigma_{UTS} = 0.7$), even at such a high yield strength in the post-yield region. All of these ensure a large safety margin against fracture, which is vital for reliability in engineering applications. The Al7Ti7 alloy has an extremely high value of $\sigma_{UTS} \times EL_T$ (72 GPa %) when compared other high-performance alloys at room temperature (Fig. 3B) (*2, 4, 5, 8, 11, 13, 14, 19, 21, 22*).

We attribute the pronounced increase in yield strengths to the precipitation hardening by these high-density L1$_2$-type MCINPs (*16*). The superb work-hardening capacity accounts for the large ductility (Fig. 4). Unlike traditional alloys, our MCINPS alloys exhibit the distinctive multiple-stage work-hardening behaviors responsible for different deformation stabilities. Both alloys have a gradual decrease in the work-hardening rate during the early strain up to 22% because of dislocation-controlled plastic deformation processes (*13*). Plastic instability onset gener-

ates necking in the Al8Ti6 alloy upon further straining. The Al7Ti7 alloy, by contrast, has a markedly different deformation behavior as the work hardening continues at larger strains. The instantaneous work-hardening exponent n in this stage shows a linear increase with a high value of 0.43 (Fig. 4B), which implies the onset of an additional deformation mode, enabling an extended uniform deformation to be sustained.

With the aim of deciphering the origin of the unusual work-hardening behavior of the Al7Ti7 alloy, we carefully investigated the dynamic evolution of deformation substructures at different strains with TEM (Fig. 4C). At the true strain of ~10%, the deformation was dominated by the planar slip of dislocations along the {111} primary slip planes, similar to that observed in most fcc-type alloys (*23–25*). As the true strain increases to ~22%, we observed well-developed HDDWs along the primary slip systems. The formation of these directional dislocation substructures (dislocation arrays and HDDWs) produced a long-range back stress that makes dislocations in the interwall space difficult to move through them, leading to an increased work-hardening response (*26–28*). Moreover, we observed wavy slips in the interwall space, indicating that the dislocation cross-slip is effectively activated at this stage. The intensive polyslips of dislocations are helpful for relieving the stress concentration on the {111} primary slip planes. Meanwhile, the progressive accumulation of these in-directional dislocations and their mutual interactions produced a pronounced forest dislocation hardening, i.e., the short-range effective stress hardening (*29–32*). We conducted tensile load-unload-reload tests to further quantify the dynamic evolutions of the work-hardening responses and associated flow stress partitioning behaviors (fig. S14). We observed a large increase in short-range effective stress, the strengthening contribution of which is almost identical to that of the long-range back stress hardening. Therefore, the high work hardening of the Al7Ti7 alloy within this stage originates from both the back stress hardening and forest dislocation hardening, which enables this alloy to maintain an unusually higher work-hardening state without local necking. By contrast, as for the true strain of ~22%, the dislocation structure of the Al8Ti6 alloy is mainly dominated by the planar-slip dislocations along the {111} primary slip planes (fig. S8). The resultant long-range back stress hardening is comparable to that of the Al7Ti7 alloy, accompanied with a lower increase in effective stress. We ascribe the inferior work-hardening response of the Al8Ti6 alloy to an insufficient effective stress hardening, leading to a relatively earlier onset of plastic instability.

With the further deformation to the true strain in the range of 28%~38% for the Al7Ti7 alloy, the main deformation characteristics are deformation-induced microbands. We detected neither mechanical twinning nor transformation-induced martensite, which are generally observed in other ductile-disordered alloys (*2, 11*). We believe

Fig. 4. Multistage work-hardening behaviors and deformation micromechanisms of the MCINPS alloys at ambient temperature. (**A**) Work-hardening rate curves of the MCINPS alloys. (**B**) Dynamic change of the work-hardening exponent (i.e., the instantaneous work-hardening exponent) within the uniform deformation process of the MCINPS alloys. (**C**) Dynamic evolution of the deformation substructures of the Al7Ti7 alloy with increasing tensile loading.
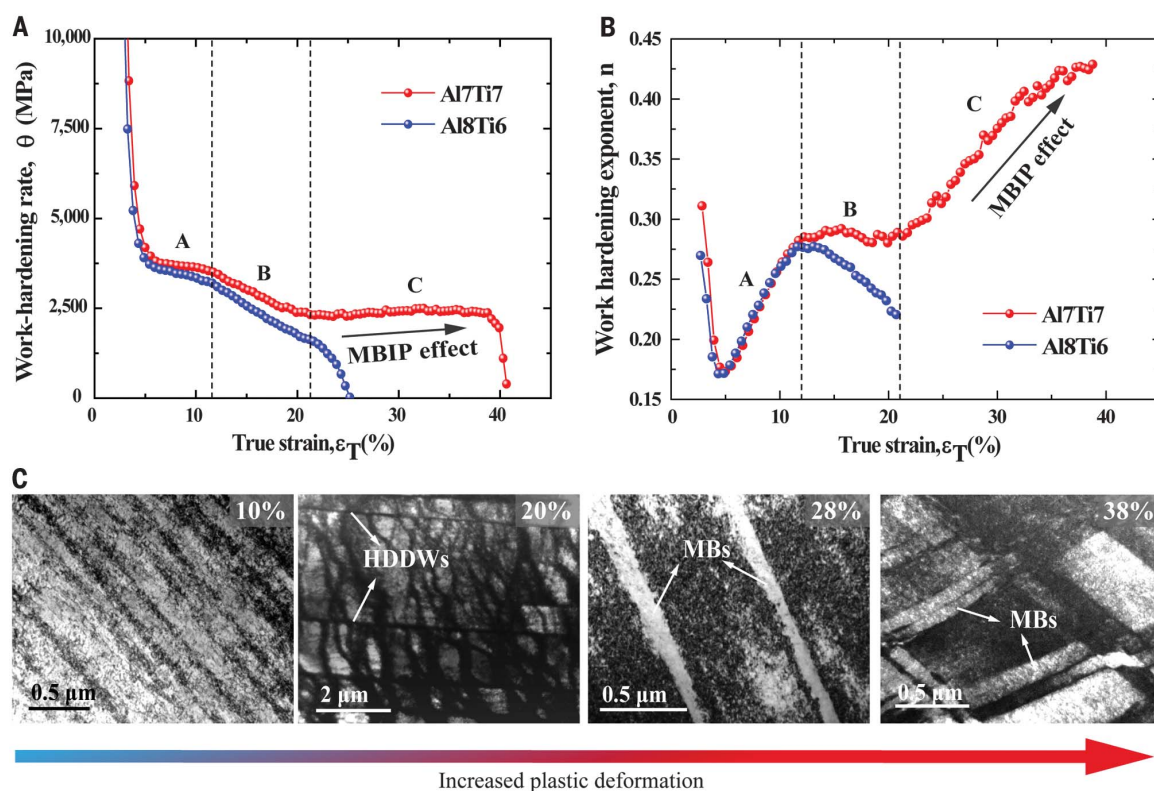
their absence is due to the medium to high stacking fault energies of the matrix alloy (*33, 34*). Moreover, the formation of such high-density MCINPs will greatly reduce the spacing size of the matrix channel down to a much finer scale of only several nanometers, which in turn further increases the resolved stress for twin formation (*35*). Under these restrictions, the microbands act as another important deformation mode to provide an additional work-hardening source to accommodate the imposed strain, leading to an exceptional plastic stability at the high-strength level. Different from the shear-bands' softening effects observed in metallic glasses and nanotwinned alloys (*36, 37*), the deformation-induced microbands, similar to the low-angle grain boundaries (fig. S9), are an important ductilizing mechanism to control the deformation stability of high-Mn alloys, namely the so-called microband-induced plasticity (MBIP) effect (*38–40*). By introducing a high-density MCINP in the Al7Ti7 alloy, we engineered the MBIP effect into the Mn-free nanostructured alloys. The formation of these microbands can generate a large increase in back stress hardening (fig. S14D), which is conducive to maintain the work-hardening capacity in the Al7Ti7 alloy for a continuous and stabilized plastic deformation. Moreover, the grain subdivision and refinement induced by these dislocation substructures further contribute to the strength enhancement because of the dynamic Hall-Petch effect (*38, 41*). The relatively weaker microband-forming ability of the Al8Ti6 alloy might be ascribed to its lower dislocation accumulation in the early stage, in which the internal stress is insufficient to activate

the cross-slip of dislocations as well as the subsequent formation of microbands (*25, 41–44*). Although we observed some microbands in the necking region (fig. S15), the resulting strain hardening in Al8Ti6 comes too late to compensate for the decrease of load-carrying capability caused by the geometric softening.

The coherent strengthening by the $L1_2$-type Ni_3Al (namely, the γ' phase) has been extensively investigated in Ni-base superalloys (*19*). However, most previous Ni_3Al phases are compositionally simple and contain a lower level of ternary elements, and the resulting superalloys show serious ductility reductions with increasing strengths (fig. S10). The multicomponent nature associated with the improved intrinsic mechanical properties of the MCINPs is the structural origin that primarily accounts for the specific mechanical properties of our MCINPS alloys. Several major contributions from the MCINPs account for the surprising ductility improvement for the alloys. First, according to the physical-metallurgy principle of ordered Ni_3Al alloys, macro-alloying with Fe and Co decreases the ordering energy and improves the intrinsic ductility (*6, 45, 46*), whereas a high level of the Al content leads to a serious environmental embrittlement when tested in air (*6, 7*). For instance, an addition of 15 at % Fe improved the ductility to ~9% of normally brittle Ni_3Al (*6*). A notable example of environmental embrittlement is the decrease in ductility of boron-doped Ni_3Al from 50% to 5% in air if the Al content is increased from 24 to 25 at %. Ti doping in our alloys results in decreased Al content and largely reduces the environmental embrittlement. The

higher Ti/Al ratio also promotes a substantial increase in the antiphase boundaries energy and a higher work-hardening because of the generation of dislocations cross-slip (*47*), which in turn favors the activation of microbands and produces an extended uniform deformation (*43, 44*). The optimum level of Ti in these alloys is determined in the range of 6.5 to 7.5 at %, and the excessive Ti additions will promote the formation of more brittle $L2_1$ particles at grain boundaries, resulting in an intergranular fracture. The potential grain-boundary embrittlement can even be eliminated by further tailoring of boron additions and/or processing conditions. Second, the low lattice misfit enables the MCINP to be stabilized at the nanoscale and uniformly distributed without heterogeneous coarsening, which effectively reduces the stress-strain concentrations at local regions and suppresses the nucleation of microcracks during deformation (*8, 18*). Moreover, from the perspective of electronic structure, small valence electron concentration values (~8.0) of the MCINP prevent the transformation from the ductile ordered cubic phase to the brittle hexagonal phase (such as η-Ni_3Ti) (*48*). For more clarity, we carefully evaluated the bulk mechanical properties of our present multicomponent $L1_2$ alloys, in which the chemical compositions are based on the APT analysis of the Al7Ti7 alloy (Fig. 2C). As expected, the present multicomponent $L1_2$ alloy is substantially stronger and more ductile than the simple Ni_3Al (*49*), exhibiting a ductility of ~40%, a yield strength of ~600 MPa, and also an excellent stain-hardening ability of about ~2.1 GPa (fig. S11). The incorporation of these strong and ductile MCINPs

allows us to not only effectively impede the dislocation motion for strengthening but also increase the damage tolerance and dislocation storage of the alloys.

In conclusion, we proposed an innovative alloy design strategy by engineering high-density MCINPs in complex alloy systems to achieve superb mechanical properties at ambient temperature. We demonstrated experimentally that the MCINPS alloys are simultaneously ultrastrong and ductile, with no strength-ductility trade-off and plastic instability. This alloy design strategy can also be feasibly applied to many other alloy systems, such as nanostructured alloys, steels, superalloys, and also HEAs, to achieve desired and enhanced properties for specific applications. The resulting new-generation complex alloys could lead to superior structural properties, which are of both great fundamental and applied importance for advanced engineering applications involving automobiles, bullet trains, cryogenic devices, and aircraft and aeronautic systems.

REFERENCES AND NOTES

1. R. O. Ritchie, *Nat. Mater.* **10**, 817–822 (2011).
2. Z. Li, K. G. Pradeep, Y. Deng, D. Raabe, C. C. Tasan, *Nature* **534**, 227–230 (2016).
3. R. Liu, Z. J. Zhang, L. L. Li, X. H. An, Z. F. Zhang, *Sci. Rep.* **5**, 9550 (2015).
4. S. H. Kim, H. Kim, N. J. Kim, *Nature* **518**, 77–79 (2015).
5. Z. B. Jiao, J. H. Luan, M. K. Miller, C. T. Liu, *Acta Mater.* **97**, 58–67 (2015).
6. N. Stoloff, *Int. Mater. Rev.* **34**, 153–184 (1989).
7. E. P. George, C. T. Liu, D. Pope, *Phys. Status Solidi* **160**, 517–529 (1997).
8. S. Jiang et al., *Nature* **544**, 460–464 (2017).
9. J. W. Yeh et al., *Adv. Eng. Mater.* **6**, 299–303 (2004).
10. O. N. Senkov, J. D. Miller, D. B. Miracle, C. Woodward, *Nat. Commun.* **6**, 6529 (2015).
11. B. Gludovatz et al., *Science* **345**, 1153–1158 (2014).
12. Z. Wu, H. Bei, G. M. Pharr, E. P. George, *Acta Mater.* **81**, 428–441 (2014).
13. W. H. Liu et al., *Acta Mater.* **116**, 332–342 (2016).
14. J. Y. He et al., *Acta Mater.* **102**, 187–196 (2016).
15. B. Gwalani et al., *Mater. Des.* **121**, 254–260 (2017).
16. Materials and methods are available as supplementary materials.
17. K. Lu, *Nat. Rev. Mater.* **1**, 16019 (2016).
18. R. C. Reed, C. M. F. Rae, in *Physical Metallurgy of the Nickel-Based Superalloys* (Elsevier, 2014), pp. 2215–2290.
19. B. Geddes, H. Leon, X. Huang, *Superalloys: alloying and performance*. (Asm International, 2010).
20. Y. I. Ustinovshikov, I. N. Shabanova, N. V. Lomova, *J. Adv. Microsc. Res.* **8**, 27–32 (2013).
21. B. B. He et al., *Science* **357**, 1029–1032 (2017).
22. D. Raabe, D. Ponge, O. Dmitrieva, B. Sander, *Scr. Mater.* **60**, 1141–1144 (2009).
23. B. Gludovatz et al., *Nat. Commun.* **7**, 10602 (2016).
24. D. Kuhlmann-Wilsdorf, *Philos. Mag. A Phys. Condens. Matter Struct. Defects Mech. Prop.* **79**, 955–1008 (1999).
25. B. Ma, C. Li, J. Zheng, Y. Song, Y. Han, *Mater. Des.* **92**, 313–321 (2016).
26. X. Hu et al., *Metall. Mater. Trans., A Phys. Metall. Mater. Sci.* **48**, 3943–3950 (2017).
27. X. Wu et al., *Proc. Natl. Acad. Sci. U.S.A.* **112**, 14501–14505 (2015).
28. M. Yang, Y. Pan, F. Yuan, Y. Zhu, X. Wu, *Mater. Res. Lett.* **4**, 145–151 (2016).
29. C. Keller, E. Hug, X. Feaugas, *Int. J. Plast.* **27**, 635–654 (2011).
30. C. Keller, M. Margulies, Z. Hadjem-Hamouche, I. Guillot, *Mater. Sci. Eng. A* **527**, 6758–6764 (2010).
31. Y. Tang et al., *Metals (Basel)* **8**, 444 (2018).
32. A. Vattré, B. Devincre, A. Roos, *Intermetallics* **17**, 988–994 (2009).
33. S. Zhao, G. M. Stocks, Y. Zhang, *Acta Mater.* **134**, 334–345 (2017).
34. X. Xie, G. Chen, P. McHugh, J. Tien, *Scr. Metall.* **16**, 483–488 (1982).
35. L. Murr, A. Ayala, C. Niou, *Mater. Sci. Eng. A* **216**, 69–79 (1996).
36. G. Wu, K. C. Chan, L. Zhu, L. Sun, J. Lu, *Nature* **545**, 80–83 (2017).
37. C. Hong, N. Tao, X. Huang, K. Lu, *Acta Mater.* **58**, 3103–3116 (2010).
38. J. D. Yoo, K.-T. Park, *Mater. Sci. Eng. A* **496**, 417–424 (2008).
39. W. Song, T. Ingendahl, W. Bleck, *Acta Metall. Engl. Lett.* **27**, 546–556 (2014).
40. Z. Wang et al., *Acta Mater.* **120**, 228–239 (2016).
41. D. Hughes, *Acta Metall. Mater.* **41**, 1421–1430 (1993).
42. I. Gutierrez-Urrutia, D. Raabe, *Scr. Mater.* **69**, 53–56 (2013).
43. P. Jackson, *Scr. Metall.* **17**, 199–202 (1983).
44. J. Huang, G. Gray III, *Acta Metall.* **37**, 3335–3347 (1989).
45. A. Chiba, S. Hanada, S. Watanabe, *Mater. Sci. Eng. A* **152**, 108–113 (1992).
46. C. Meng, J. Guo, Z. Hu, *J. Mater. Sci. Technol.* **10**, 279–284 (1994).
47. D. Raynor, J. Silcock, *Met. Sci. J.* **4**, 121–130 (1970).
48. C. T. Liu, *Int. Metals Rev.* **29**, 168–194 (1984).
49. C. T. Liu, C. L. White, *MRS Proceedings* **39**, 365 (1984).